An approach for determining the liquid water distribution in a liquid-feed direct methanol fuel cell

W.W. Yang, T.S. Zhao*, R. Chen, C. Xu

Department of Mechanical Engineering, The Hong Kong University of Science and Technology, Clear Water Bay, Kowloon, Hong Kong SAR, China

ABSTRACT

In determining the liquid water distribution in the anode (or the cathode) diffusion medium of a liquid-feed direct methanol fuel cell (DMFC) with a conventional two-phase mass transport model, a current-independent liquid saturation boundary condition at the interface between the anode flow channel and diffusion layer (DL) (or at the interface between the cathode flow channel and cathode DL) needs to be assumed. The numerical results resulting from such a boundary condition cannot realistically reveal the liquid distribution in the porous region, as the liquid saturation at the interface between the flow channel and DL varies with current density. In this work, we propose a simple theoretical approach that is combined with the in situ measured water-crossover flux in the DMFC to determine the liquid saturation in the anode catalyst layer (CL) and in the cathode CL. The determined liquid saturation in the anode CL (or in the cathode CL) can then be used as a known boundary condition to determine the water distribution in the anode DL (or in the cathode DL) with a two-phase mass transport model. The numerical results show that the water distribution becomes much more realistic than those predicted with the assumed boundary condition at the interface between the flow channel and DL.

© 2009 Elsevier B.V. All rights reserved.

1. Introduction

The generation, transport and removal of water in the cathode and the gas carbon dioxide in the anode are two key mass transport processes in an operating direct methanol fuel cell (DMFC). Liquid water accumulated in the cathode diffusion medium and in the flow channel impedes oxygen transport to the catalyst layer, restrains the oxygen reduction reaction, and thus deteriorates the cell performance and its stability [1,2]. Gas evolution in the DMFC anode affects both the through- and in-plane transport of reactants (methanol and water), making it difficult to distribute uniformly the reactants over the electrode and maintain an adequate methanol concentration in the anode catalyst layer (CL) that can maximize cell performance [3–5]. To improve the cell performance, the supply of reactants and the removal of products on both the anode and cathode need to be well managed, which demands a better understanding of the liquid-gas two-phase transport in the DMFC.

The visualization of the in situ water data in each constituent component of the DMFC is crucial to understanding the nature of water transport. Since the fuel cell is not transparent to visible light, other forms of penetrating radiation, for example, X-rays, neutrons (NR), and nuclear magnetic resonance (NMR), must be used. NR is

capable of imaging the liquid accumulation in the opaque porous medium owing to the high sensitivity of neutron beams to the water molecular. Unfortunately, only planar integrals of water content can be obtained and it is difficult to resolve the water distribution across the thickness of the fuel cell [6–8]. NMR has been used to probe the liquid water transport in the polymer electrolyte fuel cells (PEFCs) [9,10]. However, the presence of magnetically inductive materials, like carbon, makes NMR unsuitable for carbon-based components. Recently, X-ray microtomography has been introduced to probe the liquid transport in the diffusion medium of PEFCs [11,12]. Nevertheless, limited by the imaging resolution, it is still difficult to image the liquid distribution in a porous medium with small pore size. It is worth mentioning that although significant efforts have been made to visualize the water distribution in PEFCs, no work on the in situ imaging of the liquid water distribution in liquid-feed DMFCs has been reported, mainly due to the difficulty caused by the presence of water at both the anode and the cathode in this type of fuel cell.

Compared with previous experimental investigations of the liquid water distribution in fuel cells, much more studies have been devoted to numerical visualization of the water distribution in both PEFCs [13–18] and DMFCs [19–27] based on two-phase mass transport models. The accuracy of a numerical investigation of a physical problem depends not only on a robust model formulation but also on realistic boundary conditions [28]. For instance, in determining the liquid water distribution in the anode (or the cathode) diffusion medium of a liquid-feed DMFC with a conventional two-phase
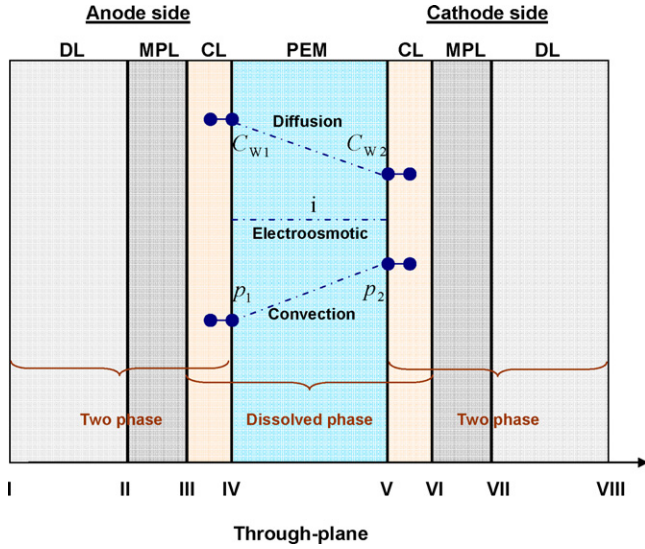
Fig. 1. Schematic illustration of water transport through membrane electrode assembly of DMFC.

mass transport model, a current density-independent liquid saturation boundary condition at the interface between the anode flow channel and diffusion layer (DL) (or at the interface between the cathode flow channel and cathode DL) needs to be assumed. The predictions resulting from such an assumed boundary condition cannot realistically reveal the water transport and distribution in the porous regions of the DMFC, as the liquid saturation at the flow channel/DL interface varies with current density and other operating conditions.

To avoid the use of an unrealistic boundary condition in simulating water transport in a DMFC with a two-phase mass transport model, a simple theoretical approach is proposed in this study. It is combined with the in situ measured water-crossover flux in the DMFC to determine the liquid saturation in both the anode and the cathode CLs. The determined liquid saturation in the anode CL (or in the cathode CL) can then be used as a boundary condition to determine the water distribution in the anode DL (or in the cathode DL).

2. Analytical

As shown schematically in Fig. 1, the dissolved water in a DMFC membrane can be transported from the anode to cathode as a result of three transport mechanisms: electro-osmotic drag due to proton transport, diffusion due to a water concentration gradient, and convection due to a hydraulic pressure gradient [29–31]. The water flux by electro-osmotic drag can be determined from:

$$J_{eo} = n_d \frac{i}{F} \tag{1}$$

where i is the cell current density and F is Faraday's constant; the term n_d represents the electro-osmotic drag coefficient that is related to the water content λ in the membrane by [16]:

$$n_d = \frac{2.5}{22}\lambda \tag{2}$$

The water flux by diffusion resulting from a water concentration difference across the membrane can be expressed as

$$J_{diff} = -D_{w,N}\nabla \cdot c_w \tag{3}$$

where $D_{W,N}$ is the diffusion coefficient of the dissolved water in the membrane, which depends on the water content in the membrane as listed in Table 1; the concentration of dissolved water c_w

is related to the water content λ by:

$$c_w = \frac{\rho_{dry}\lambda}{EW} \tag{4}$$

where ρ_{dry} and EW denote, respectively, the density of a dry membrane and the equivalent weight of ionomer in the membrane.

The water flux by convection is given by [29]:

$$J_c = \frac{K_{mem}\rho_l(p_{l,a} - p_{l,c})}{\mu_l M_{H_2O}\delta_{mem}} \tag{5}$$

where K_{mem}, δ_{mem}, ρ_l, μ_l and M_{H_2O} represent, respectively, the hydraulic permeability of the membrane, the thickness of the membrane, the water density, the viscosity of liquid water and the molecular weight of water; $p_{l,a}$ and $p_{l,c}$ denote, respectively, the liquid pressure at the anode and cathode surfaces towards the membrane. Note that $p_{l,a}$ is almost the same as that in the anode flow channel, as the liquid flow velocity through the anode DL is typically small, whereas $p_{l,c}$ is related to the gas pressure and the capillary pressure in the cathode CL by:

$$p_c = p_{g,c} - p_{l,c} = \sigma \cos\theta_{ccl} \left(\frac{\varepsilon_{ccl}}{K_{ccl}}\right)^{1/2} J(s_{ccl}) \tag{6}$$

where K_{cc1}, σ and θ_{cc1} are, respectively, the permeability of the cathode CL, the surface tension and the contact angle of the cathode CL; $p_{g,c}$ is the gas pressure at the cathode surface towards the membrane, which is nearly the same as that in the cathode flow channel; the term S_{cc1} is the liquid saturation (i.e., the volume fraction of liquid water filled pores) and the term $J(s)$ is the Leverett function and given by:

$$J(s)=\begin{cases} 1.417(1-s)-2.120(1-s)^2+1.263(1-s)^3 & 0 < \theta \leq 90° \\ 1.417s-2.120s^2+1.263s^3 & 90° < \theta < 180° \end{cases} \tag{7}$$

Substituting Eq. (6) into Eq. (5) and assuming that the DMFC operates at the same inlet pressure at both the anode and the cathode, yields:

$$J_c = \frac{K_{mem}\rho_l\sigma\cos\theta_{ccl}}{\mu_l M_{H_2O}\delta_{mem}} \left(\frac{\varepsilon_{ccl}}{K_{ccl}}\right)^{1/2} J(s_{ccl}) \tag{8}$$

Eq. (8) indicates that even though the DMFC operates at the same pressure at the anode and the cathode, a hydrophobic cathode diffusion medium ($\cos\theta < 0$) can cause water convection from the cathode to the anode, which is termed the back-flow flux.

In summary, the total flux of water crossover can be obtained by summing up Eqs. (1), (3) and (8) to give:

$$J_{wc} = n_d \frac{i}{F} - D_{w,N}\nabla \cdot c_w + \frac{K_{mem}\rho_l\sigma\cos\theta}{\mu_l M_{H_2O}\delta_{mem}} \left(\frac{\varepsilon_{ccl}}{K_{ccl}}\right)^{1/2} J(s_{ccl}) \tag{9}$$

Eq. (9) indicates that the water-crossover flux depends on the current density, the dissolved water concentration and its gradient across the membrane, and the liquid water saturation in the cathode CL. The dissolved water concentration in the anode CL can be related to the local liquid water saturation and is affected by the local gas void fraction, which depends on the generation rate of gas CO_2 in the anode CL and the removal capability of gas CO_2 from the anode CL. Similarly, the dissolved water concentration in the cathode CL can also be related to the local liquid water saturation in the cathode CL, which depends on the generation rate of water in the cathode CL and the removal capability of liquid water from the cathode CL. Under a condition of phase equilibrium between the water dissolved in the ionomer in each CL and the liquid water in the pores of each CL, the

Table 1
Cell geometric dimensions, operating parameter and physicochemical properties.

Parameters		Symbols	Value	Unit	Ref.
Thickness, porosity, permeabilityand contact angle	Anode DL	$\delta_{adl}, \varepsilon_{adl}, K_{adl}, \theta_{adl}$	2.6×10^{-4}, 0.75, 1.0×10^{-12}, 110	m, -, m^2, $^\circ$	
	Anode MPL	$\delta_{ampl}, \varepsilon_{ampl}, K_{ampl}, \theta_{ampl}$	0.1×10^{-4}, 0.3, 5.0×10^{-13}, 120	m, -, m^2, $^\circ$	
	Anode CL	$\delta_{acl}, \varepsilon_{acl}, K_{acl}, \theta_{acl}$	0.1×10^{-4}, 0.3, 3.0×10^{-14}, 95	m, -, m^2, $^\circ$	
	Membrane	$\delta_{mem}, \varepsilon_{mem}, K_{mem}$	0.5×10^{-14}, 0.3, 2.0×10^{-18}	m, -, m^2	
	Cathode CL	$\delta_{ccl}, \varepsilon_{ccl}, K_{ccl}, \theta_{ccl}$	0.1×10^{-4}, 0.3, 3.0×10^{-14}, 95	m, -, m^2, $^\circ$	
	Cathode MPL	$\delta_{cmpl}, \varepsilon_{cmpl}, K_{cmpl}, \theta_{cmpl}$	0.1×10^{-4}, 0.3, 5.0×10^{-13}, 120	m, -, m^2, $^\circ$	
	Cathode DL	$\delta_{cdl}, \varepsilon_{cdl}, K_{cdl}, \theta_{cdl}$	2.6×10^{-4}, 0.75, 1.0×10^{-12}, 110	m, -, m^2, $^\circ$	
Cell temperature		T	343.15	K	[29]
Anode and cathode inlet pressure		p_{in}	1.013×10^5	Pa	[29]
Viscosity of gas phase		μ_g	2.03×10^{-5}	kg m^{-1} s^{-1}	[17]
Viscosity of liquid phase		μ_l	4.05×10^{-4}	kg m^{-1} s^{-1}	[17]
Equilibrium water contents when the polymer electrolyte is in phase equilibrium with the water–vapor-saturated gas		λ_{WV}^{eq}	13.06 (70 $^\circ$C)	–	[30]
Equilibrium water contents when the polymer electrolyte is in phase equilibrium with		λ_l^{eq}	22	–	[32]
Diffusivity of water in the membrane		$D_{W,N}$	4.17×10^{-8} $\lambda(161 e^{-\lambda} + 1)e^{-2436/T}$	m^2 s^{-1}	[30]
Surface tension		σ	0.0644	N m^{-1}	[17]
Equivalent weight of ionomer		EW	1.1	kg mol^{-1}	[34]
Dry membrane density		ρ_{dry}	1980	kg m^3	[34]

dissolved water concentration in both the anode and the cathode CL is related to liquid saturation by [31]:

$$\lambda = (1 - s)\lambda_{WV}^{eq} + s\lambda_l^{eq} \qquad (10)$$

where λ_{WV}^{eq} and λ_l^{eq} denote the equilibrium water concentration in the ionomer when the ionomer is in phase equilibrium with the water–vapor-saturated gas [30] and liquid water [32,33], respectively.

Mathematically, Eq. (9) can be rewritten as

$$\alpha(\lambda)\lambda' + \beta(\lambda) + \gamma(\lambda_{ccl}) + J_{wc} = 0 \qquad (11)$$

where

$$\alpha(\lambda) = \frac{D_{W,N}(\lambda)\rho_{dry}}{EW} \qquad (11a)$$

$$\beta(\lambda) = -\frac{2.5i\lambda}{22F} \qquad (11b)$$

and

$$\gamma(\lambda_{ccl}) = -\frac{K_{mem}\rho_l\sigma \cos\theta}{\mu_l M_{H_2O}\delta_{mem}}\left(\frac{\varepsilon_{ccl}}{K_{ccl}}\right)^{1/2}J(s_{ccl}) \qquad (11c)$$

where λ' is the water content gradient across the membrane. As Eq. (11) is a first-order ordinary differential equation, at a given current density and for a given water-crossover flux, J_{wc}, the distribution of water content in the membrane can be determined by solving Eq. (11) provided that the water content boundary condition on either side of the membrane (Interface IV or V, Fig. 1) is known.

In summary, for a given water-crossover flux, J_{wc}, when the liquid saturation in either the anode CL or the cathode CL is known (which can be converted to the water content according to Eq. (10)), the liquid saturation in the other side and the water-content distribution across the membrane can be determined by solving Eq. (11). In this work, the water-crossover flux, J_{wc}, comes from a previous study by Xu and Zhao [29], who measured the water-crossover flux in typical operating DMFCs with different cathode designs under different operating conditions. The key now is how to specify an appropriate boundary condition of water content at the anode surface or the cathode surface of the membrane.

3. Results and discussion

3.1. Determination of liquid saturation in anode CL

This section addresses the determination of the liquid saturation in the anode CL and the distribution of water content across the membrane. To this end, the water-crossover flux and the liquid saturation in the cathode CL are needed.

Fig. 2 shows the variation in the total water flux (due to water generation and water crossover) and the water-crossover flux with current density for various cathode DL designs [29]. Note that the solid symbols represent the total water flux, while the hollow symbols represent the water-crossover flux. The total water flux corresponding to each cathode DL design is almost independent of the current density in the low-current density region (<200 mA cm^{-2}). This observation, suggests that, for a given cath-
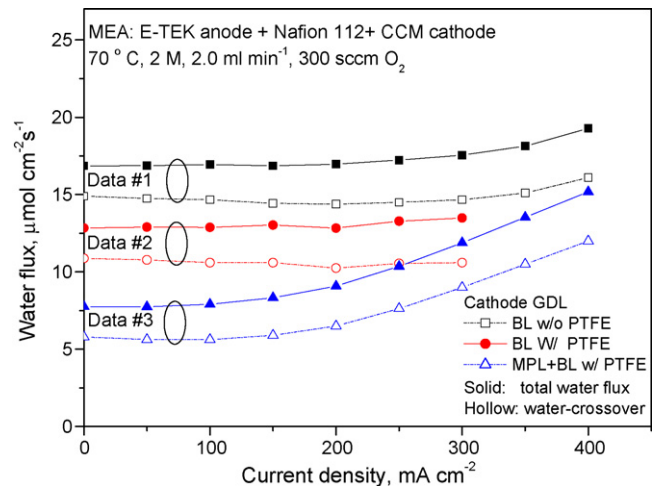
Fig. 2. Total water flux and water-crossover flux to DMFC cathode with various cathode DL designs measured by Xu and Zhao [29].
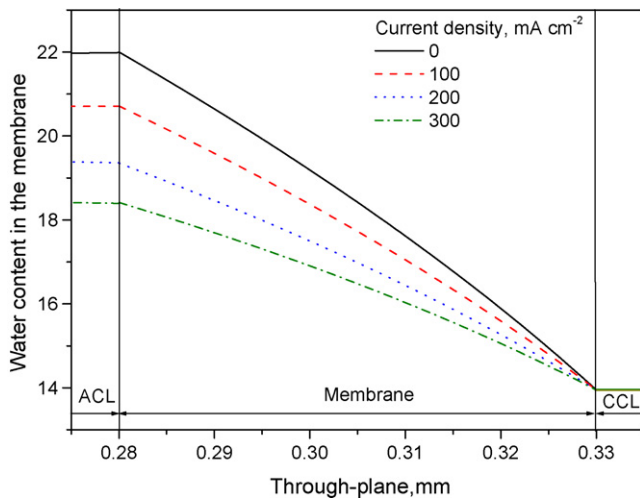
Fig. 3. Profiles of water content across membrane at different current densities.

Fig. 4. Comparison between liquid saturation in anode CL determined by present approach based on data shown in Fig. 2 and that predicted by model with assumed boundary condition.

ode design and at a given gas flow rate, the water distribution in the DMFC cathode CL and DL depends on the total water flux removed from the cathode only, but not on the current density. Hence, the liquid saturation in the cathode CL at different current densities ($<200\,mA\,cm^{-2}$) is approximately the same as that under the open-circuit condition (OCC, i.e., $i=0$) for the same total water flux. Also note that as no gas CO_2 is produced under the OCC, the liquid saturation in the anode CL remains at 1.0 (pure liquid). According to Eq. (10), the water content corresponding to a liquid saturation of 1.0 is 22.0. With this understanding, setting $i=0$ (under the OCC), substituting the water-crossover flux for each cathode DL design into Eq. (11), specifying the water content boundary condition at the anode surface of the membrane to be 22.0, and solving Eq. (11) will result in the water content in the cathode CL and the distribution of water content across the membrane. Note that the obtained water content in the cathode CL does not change at the current densities lower than $200\,mA\,cm^{-2}$. This water content can now be used as the cathode boundary condition of Eq. (11) for determining the water content in the anode CL and across the membrane for each water-crossover flux at different current densities ($<200\,mA\,cm^{-2}$).

Fig. 3 presents the water content profiles across the membrane at different current densities, which are determined based on the water-crossover flux marked as Data #2 in Fig. 2. With increase in the current density, the water concentration in the anode CL decreases significantly, as the liquid saturation level in the anode CL decreases with increasing CO_2 generation rate. The liquid saturation in the anode CL determined based on all the data shown in Fig. 2 is displayed in Fig. 4. Interestingly, it is seen that the calculated liquid saturations in the anode CL based on all the data shown in Fig. 2 for different cathode DL designs are almost the same at a given current density, implying that the liquid (or gas) distribution in the DMFC anode is essentially independent of the cathode structure. Also, it is seen from Fig. 4 that the mean liquid saturation in the anode CL decreases with increasing current density. For instance, the mean liquid saturation in the anode CL is about 0.95 at $30\,mA\,cm^{-2}$, indicating that only 5% of the pore volume of the anode CL is occupied by the gas phase. The liquid saturation becomes about 0.6 at $300\,mA\,cm^{-2}$, which means that almost 40% of the pore volume in the anode CL is filled with gas at a high current density. In addition, Fig. 4 also presents the liquid saturation in the anode CL predicted by a previous model based on the theory of two-phase flow in porous media [19]. In the model, the liquid saturation at Interface I (the anode flow channel/DL interface, see Fig. 1) was assumed to be 1.0. As can be seen from Fig. 4, although the liq-
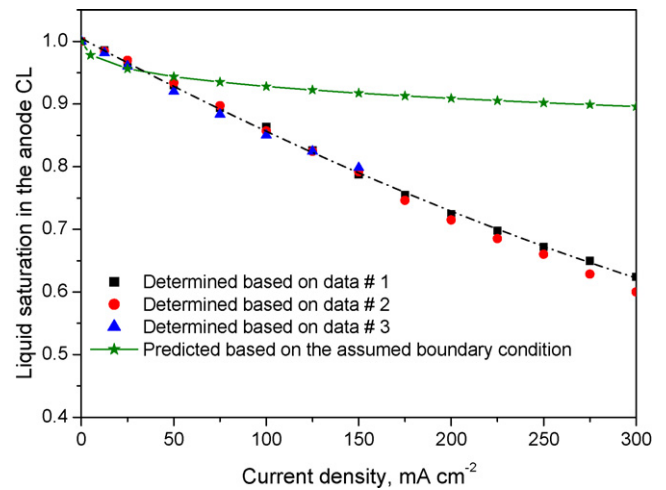
uid saturation in the anode CL predicted by the model decreases with increasing current density, the variation in the liquid saturation with the current density is rather small. Also, it is found that the mean liquid saturation predicted by the model is much higher than that determined by the present approach. This is probably due to the fact that the assumed boundary condition (i.e., $s=1.0$ at Interface I) is unrealistic, as many gas bubbles are present in the anode flow channel and cover the surface of the anode DL at high current densities, particularly in the downstream region.

3.2. Determination of liquid saturation in the anode DL

In previous studies [30,31], the distribution of liquid saturation in the anode DL was determined by assuming a boundary condition at the anode flow channel/DL interface (e.g., $s=1.0$ at Interface I). This distribution can now be obtained without invoking the past unjustified boundary condition at Interface I, but with the liquid saturation in the anode CL for the boundary condition at Interface III. The results are presented in Fig. 5 and show that the liquid saturation in the anode DL decreases significantly with increasing current density. For instance, the mean liquid saturation in the anode backing layer (BL) decreases from about 0.92 to about 0.55
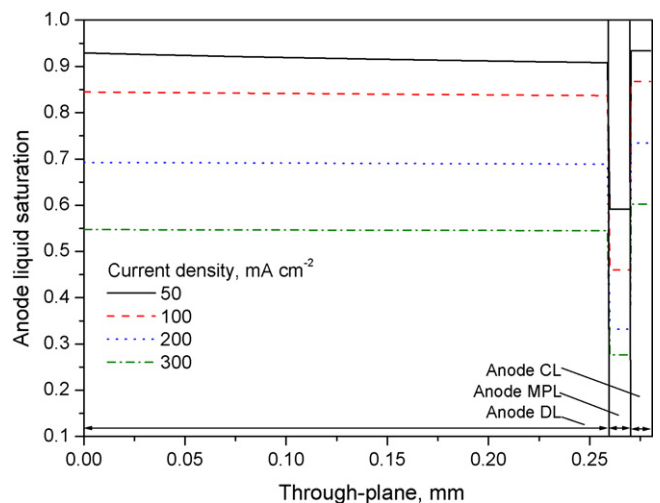

Fig. 5. Liquid saturation distribution across anode DL determined by present approach.
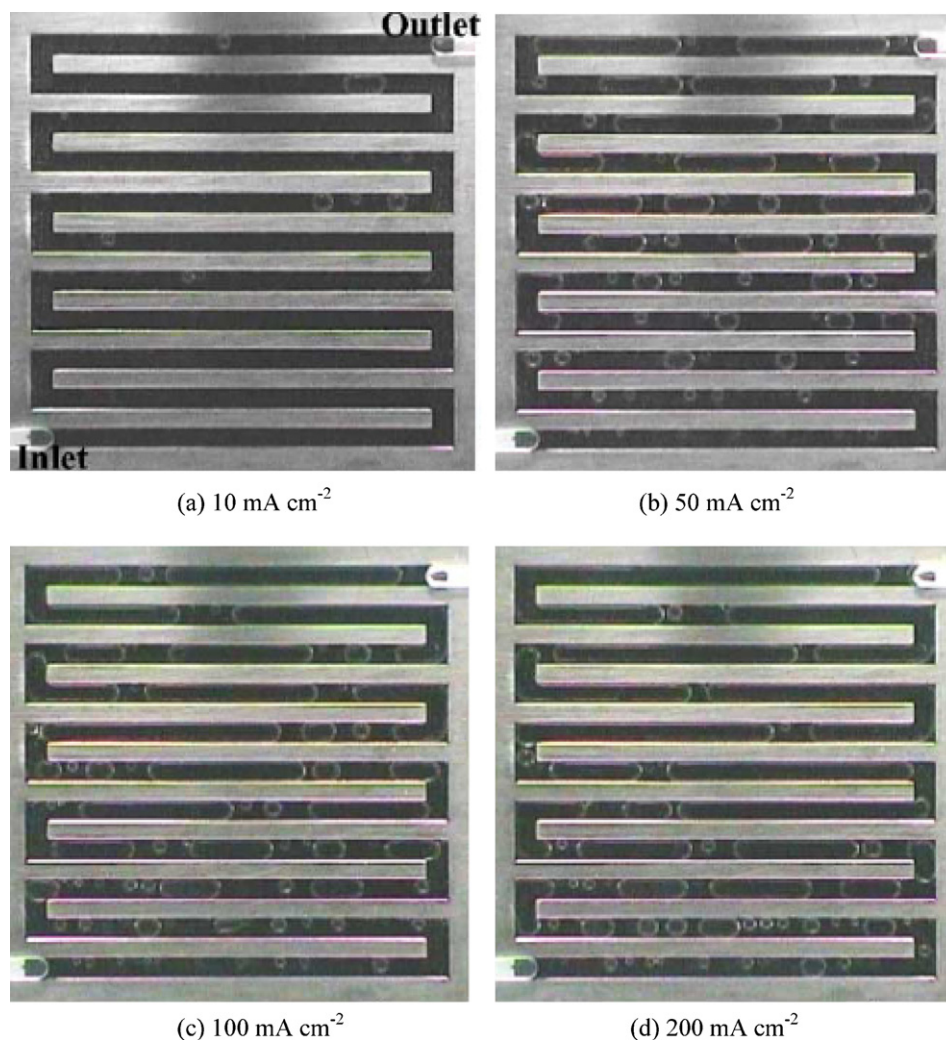
Fig. 6. Two-phase flow behaviour in anode flow-field at different current densities visualized by Yang and Zhao [3].

as the current density is increased from 50 to 300 mA cm^{-2}. More importantly, it is noticed that the liquid saturation at Interface I also decreases with increasing current density, indicating that the gas bubble coverage at Interface I increases with increasing current density. This result is consistent with a previous visual study of the bubble behaviour in the anode flow-field [3], which is displayed in Fig. 6. With increase in the current density, the gas void fraction in the anode flow field increases significantly, which consequently results in an increase in the gas coverage on the anode DL surface and a decrease in the liquid saturation at Interface I. In fact, the increase in the gas coverage on the surface of the anode DL in turn hinders the removal of gas out of the anode porous region and results in an increase in gas void fraction in the anode porous region [19,20,22,24].

For comparison with the liquid saturation distribution shown in Fig. 5, the liquid saturation distribution in the anode DL predicted by the model with the assumed boundary condition (i.e., $s = 1.0$ at Interface I) is displayed in Fig. 7. Note that setting the liquid saturation at Interface I to be 1.0 means that pure liquid travels in the flow channel without gas bubbles, which can be justified only at rather low-current densities and at extremely high flow rates. The data in Fig. 7 indicate that the use of this unrealistic boundary condition results in an overestimated liquid saturation in the anode DL and CL. Also, it is seen that the variation in the predicted liquid saturation with the current density is much smaller than that shown in Fig. 5.

3.3. Determination of liquid saturation in cathode CL

The determination of the liquid saturation in the cathode CL is based on the following understandings: (i) the water distribution in the cathode porous region is independent of current density, i.e., the water distribution determined under the OCC can represent those at different current densities; (ii) under the OCC, the liquid saturation in the anode CL is 1.0; so that the water content boundary condition at the anode of the membrane can be set to be 22.0. With this boundary condition, solving Eq. (11) for the water content for each measured water-crossover flux will result in the distribution of water content across the membrane and the water content in the cathode CL.

Fig. 8 gives the variation in the measured water-crossover flux under the OCC with oxygen flow rate for different cathode DL designs [29]. In general, the water-crossover flux increases with increasing gas flow rate, as a higher gas flow rate leads to a lower water concentration and liquid pressure at the cathode surface of the membrane. Fig. 9a presents the determined mean water content in the cathode CL corresponding to the data shown in Fig. 8. Evidently, the mean water content in the cathode CL decreases with increasing oxygen flow rate, and particularly, the cathode DL without PTFE treatment exhibits a much more rapid decrease that does the other two cases. Fig. 9b shows the mean liquid saturation in the cathode CL corresponding to the water content presented in Fig. 9a. As can be seen, at a very low oxygen flow rate, the liquid saturation
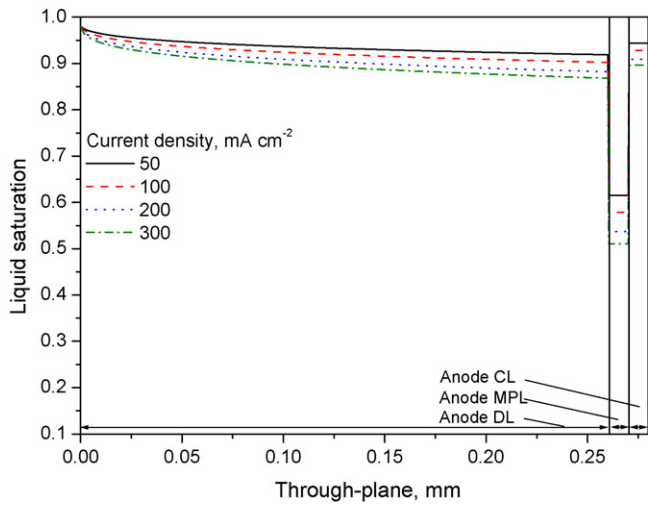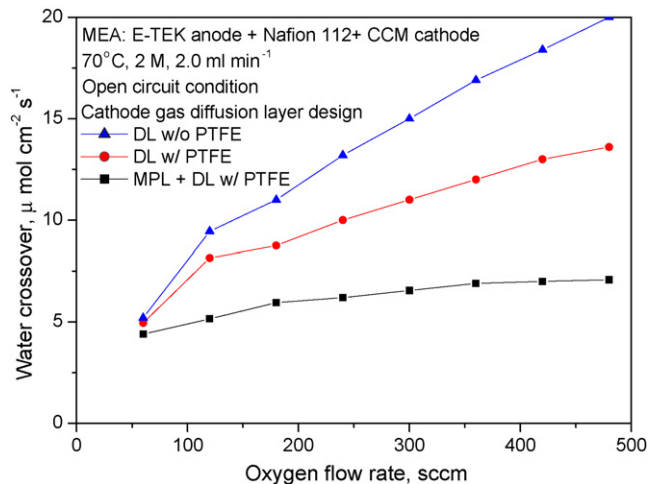
Fig. 7. Liquid saturation distribution across anode diffusion medium predicted by model with assumed boundary condition.

in the cathode CL is high; in particular the cathode DL with PTFE treatment and with a coated micro-porous layer (MPL) shows the highest liquid saturation among all the cases. With increasing the gas flow rate, the liquid saturation level in the cathode CL decreases; it even decreases to zero for the cathode DL without PTFE treatment when the oxygen flow rate is higher than 200 sccm, meaning that there is no liquid-phase water presented in the cathode CL at very high gas flow rates. This result agree with the understanding that a higher cathode gas flow rate exhibits a higher water removal ability, tending to mitigate the water flooding level in the cathode CL [29].

3.4. Determination of liquid saturation in cathode DL

In a manner similar to the anode DL, the liquid water distribution in the cathode DL can be quantified by using the two-phase model [19] when the above-determined liquid saturation in the cathode CL is used as the boundary condition at the cathode CL/DL interface (Interface VI). Fig. 10 compares the liquid saturation distribution across the cathode DL predicted by the model with the commonly assumed boundary condition (i.e., $s \approx 0$ at Interface VIII) [13,14,16,17,22,26,30,31] and the pre-determined boundary condition at Interface VI. The results were obtained for the cathode DL with MPL at an oxygen flow rate of 60 sccm shown in Fig. 8. As can

Fig. 8. Water-crossover flux to cathode for different cathode DL designs under open-circuit condition measured by Xu and Zhao [29].
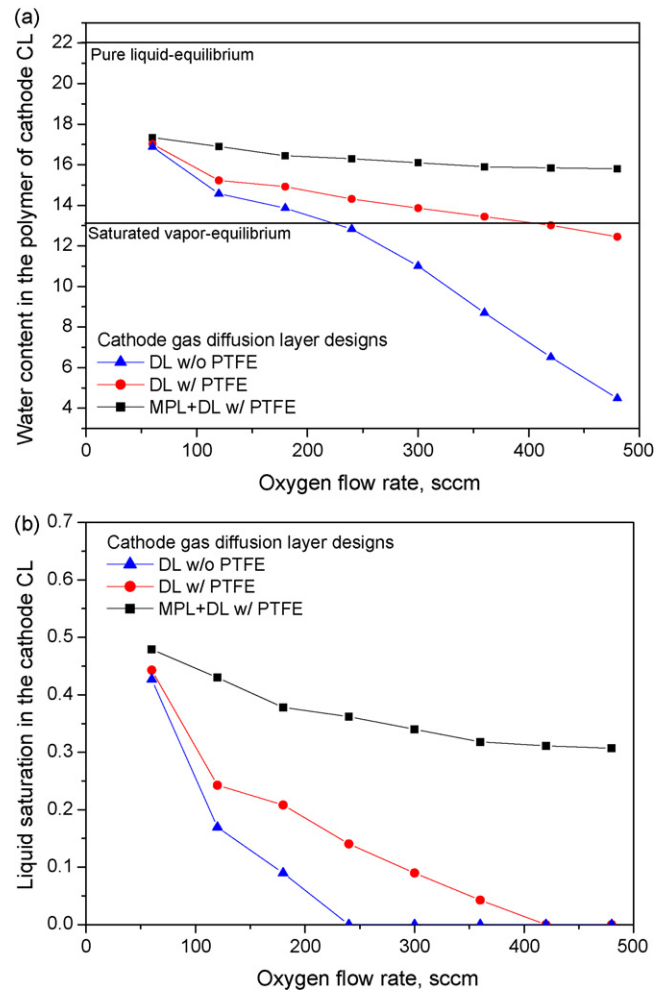
Fig. 9. Water content (a) and liquid saturation (b) in cathode CL quantified by proposed approach based on data plotted in Fig. 8.
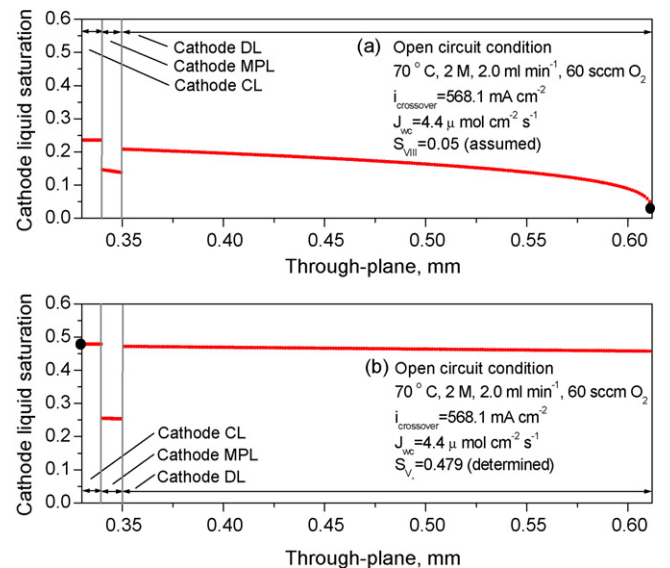
Fig. 10. Liquid saturation distribution across cathode diffusion medium (a) directly predicted by model with assumed boundary condition and (b) indirectly quantified with help of quantified liquid saturation in cathode CL.

be seen from Fig. 10a, the liquid water saturation predicted by the model with the assumed boundary condition is much lower than that predicted by the model with the determined boundary condition shown in Fig. 10b. The significant difference between the results due to the two different specifications of the boundary condition can be attributed to the following reason. In the former case, setting the liquid saturation at Interface VIII (the cathode flow channel/DL interface) to be zero can only be justified at extremely high gas flow rates such that the liquid water in the flow channel can be instantly removed and no liquid droplets or film is presented at the cathode DL surface. Practically, however, the liquid water in the flow channel and at the cathode DL surface varies with the gas flow rate. Rather than assuming an unrealistic boundary condition at the cathode flow channel/DL interface (Interface VIII), the liquid water coverage at the cathode DL surface can now be determined by the approach proposed in this work.

4. Conclusions

In this work, we propose a simple theoretical approach that is combined with the in situ measured water-crossover flux in the DMFC to determine the liquid saturation in the anode CL and in the cathode CL. The determined liquid saturation in the anode CL (or in the cathode CL) can then be used as a known boundary condition to determine the water distribution in the anode DL (or in the cathode DL) with a two-phase mass transport model, avoiding the use of the assumed boundary conditions at the flow channel/DL interface in the conventional two-phase mass transport model. The numerical results show that the water distribution determined by the present approach becomes much more realistic than that predicted with the assumed boundary condition at the flow channel/DL interface.

Acknowledgements

References

[1] C. Xu, T.S. Zhao, Electrochem. Commun. 9 (2007) 497.
[2] X.G. Yang, F.Y. Zhang, A.L. Lubawy, C.Y. Wang, Electrochem. Solid-State Lett. 7 (2004) A408.
[3] H. Yang, T.S. Zhao, Q. Ye, J. Power Sources 139 (2005) 79.
[4] C.W. Wong, T.S. Zhao, Q. Ye, J.G. Liu, J. Electrochem. Soc. 152 (2005) A1600.
[5] H. Yang, T.S. Zhao, Electrochim. Acta 50 (2005) 3243.
[6] M.A. Hickner, N.P. Siegel, K.S. Chen, D.N. Mcbrayer, D.S. Hussey, D.L. Jacobson, M. Arif, J. Electrochem. Soc. 153 (2006) A902.
[7] H. Ju, G. Luo, C.Y. Wang, J. Electrochem. Soc. 154 (2007) B218.
[8] N. Pekula, K. Heller, P.A. Chuang, A. Turhan, M.M. Mench, J.S. Brenizer, K. Ünlü, Nucl. Instrum. Methods A 542 (2005) 134.
[9] K. Teranishi, S. Tsushima, S. Hirai, J. Electrochem. Soc. 153 (2006) A664.
[10] K.W. Feindel, S.H. Bergens, R.E. Wasylishen, J. Am. Chem. Soc. 128 (2006) 14192.
[11] P.K. Sinha, P. Halleck, C.Y. Wang, Electrochem. Solid-State Lett. 9 (2006) A344.
[12] S.J. Lee, N.Y. Lim, S. Kim, G.G. Park, C.S. Kim, J. Power Sources 185 (2008) 867.
[13] D. Natarajan, T.V. Nguyen, J. Electrochem. Soc. 148 (2001) A1324.
[14] U. Pasaogullari, C.Y. Wang, J. Electrochem. Soc. 152 (2005) A380.
[15] H. Meng, C.Y. Wang, J. Electrochem. Soc. 152 (2005) A1733.
[16] G.Y. Lin, T.V. Nguyen, J. Electrochem. Soc. 153 (2006) A372.
[17] W.W. Yang, T.S. Zhao, Y.L. He, J. Power Sources 185 (2008) 765.
[18] L.X. You, H.T. Liu, J. Power Sources 155 (2006) 219.
[19] W.W. Yang, T.S. Zhao, Electrochim. Acta 52 (2007) 6125.
[20] W.W. Yang, T.S. Zhao, C. Xu, Electrochim. Acta 53 (2007) 853.
[21] Z.H. Wang, C.Y. Wang, J. Electrochem. Soc. 150 (2003) A508.
[22] W.W. Yang, T.S. Zhao, J. Power Sources 174 (2007) 136.
[23] J. Rice, A. Faghri, Int. J. Heat Mass Transf. 49 (2006) 4804.
[24] E. Birgersson, J. Nordlund, M. Vynnycky, C. Picard, G. Lindbergh, J. Electrochem. Soc. 151 (2004) A2157.
[25] J. Divisek, J. Fuhrmann, K. Gärtner, R. Jung, J. Electrochem. Soc. 150 (2003) A811.
[26] W.W. Yang, T.S. Zhao, J. Power Sources 185 (2008) 1131.
[27] G. Murgia, L. Pisani, A.K. Shukla, K. Scott, J. Electrochem. Soc. 150 (2003) A1231.
[28] K.Z. Yao, K. Karan, K.B. Mcauley, P. Oosthuizen, B. Peppley, T. Xie, Fuel Cells 4 (2004) 3.
[29] C. Xu, T.S. Zhao, J. Power Sources 168 (2007) 143.
[30] C. Xu, T.S. Zhao, W.W. Yang, J. Power Sources 178 (2008) 291.
[31] W.W. Yang, T.S. Zhao, J. Power Sources 188 (2009) 433.
[32] A.Z. Weber, J. Newman, J. Electrochem. Soc. 150 (2003) A1008.
[33] A.Z. Weber, J. Newman, J. Electrochem. Soc. 151 (2004) A311.
[34] H. Meng, C.Y. Wang, J. Electrochem. Soc. 151 (2004) A358.